

## THE BOSS EMISSION-LINE LENS SURVEY. II. INVESTIGATING MASS-DENSITY PROFILE EVOLUTION IN THE SLACS+BELLS STRONG GRAVITATIONAL LENS SAMPLE<sup>1</sup>

ADAM S. BOLTON<sup>2</sup>, JOEL R. BROWNSTEIN<sup>2</sup>, CHRISTOPHER S. KOCHANEK<sup>3</sup>, YIPING SHU<sup>2</sup>, DAVID J. SCHLEGEL<sup>4</sup>, DANIEL J. EISENSTEIN<sup>5</sup>, DAVID A. WAKE<sup>6</sup>, NATALIA CONNOLLY<sup>7</sup>, CLAUDIA MARASTON<sup>8</sup>, RYAN A. ARNESON<sup>2,9</sup>, AND BENJAMIN A. WEAVER<sup>10</sup>

*Draft version May 26, 2018*

### ABSTRACT

We present an analysis of the evolution of the central mass-density profile of massive elliptical galaxies from the SLACS and BELLS strong gravitational lens samples over the redshift interval  $z \approx 0.1$ – $0.6$ , based on the combination of strong-lensing aperture mass and stellar velocity-dispersion constraints. We find a significant trend towards steeper mass profiles (parameterized by the power-law density model with  $\rho \propto r^{-\gamma}$ ) at later cosmic times, with magnitude  $d\langle\gamma\rangle/dz = -0.60 \pm 0.15$ . We show that the combined lens-galaxy sample is consistent with a non-evolving distribution of stellar velocity dispersions. Considering possible additional dependence of  $\langle\gamma\rangle$  on lens-galaxy stellar mass, effective radius, and Sérsic index, we find marginal evidence for shallower mass profiles at higher masses and larger sizes, but with a significance that is sub-dominant to the redshift dependence. Using the results of published Monte Carlo simulations of spectroscopic lens surveys, we verify that our mass-profile evolution result cannot be explained by lensing selection biases as a function of redshift. Interpreted as a true evolutionary signal, our result suggests that major dry mergers involving off-axis trajectories play a significant role in the evolution of the average mass-density structure of massive early-type galaxies over the past 6 Gyr. We also consider an alternative non-evolutionary hypothesis based on variations in the strong-lensing measurement aperture with redshift, which would imply the detection of an “inflection zone” marking the transition between the baryon-dominated and dark-matter halo-dominated regions of the lens galaxies. Further observations of the combined SLACS+BELLS sample can constrain this picture more precisely, and enable a more detailed investigation of the multivariate dependences of galaxy mass structure across cosmic time.

*Subject headings:* galaxies: elliptical and lenticular, cD — galaxies: evolution — galaxies: structure — gravitational lensing: strong

### 1. INTRODUCTION

Massive elliptical galaxies play a starring role in both galaxy evolution and cosmology. In the former context, they are the end-products of hierarchical galaxy merging (e.g., Toomre & Toomre 1972; Schweizer 1982; White & Frenk 1991; Kauffmann et al. 1993; Cole et al.

2000), and in the latter context they are highly biased tracers of large-scale structure that are easily visible at cosmological distances (e.g., Eisenstein et al. 2005; Percival et al. 2007). Hence cosmological spectroscopic survey samples such as the luminous red galaxy sample (LRG; Eisenstein et al. 2001) of the Sloan Digital Sky Survey (SDSS; York et al. 2000) and the Baryon Oscillation Spectroscopic Survey of the SDSS-III (BOSS; Eisenstein et al. 2011; Dawson et al. 2012) provide unequaled opportunities to study massive galaxy evolution.

Important problems in massive galaxy evolution remain open, including quantifying the role of mergers in their evolution (e.g., van Dokkum et al. 1999; Khochfar & Burkert 2003; Bell et al. 2006), deducing the history of their stellar populations over cosmic time (e.g., Thomas et al. 2005; Maraston et al. 2009), and identifying the mechanism for their observed evolution in size (e.g., Daddi et al. 2005; Zirm et al. 2007; van der Wel et al. 2008; van Dokkum et al. 2008). The persistence of these and other problems is due in large part to the difficulty of making precise galaxy mass measurements at cosmological distances. Stellar mass measurements based upon integrated photometric and spectroscopic diagnostics, in addition to being insensitive to dark-matter content, are limited by uncertainties in the initial mass function and other stellar-population parameters (e.g., Conroy et al. 2009), and detailed dynamical modeling methods applicable to early-

<sup>1</sup> Based on observations made with the NASA/ESA Hubble Space Telescope, obtained at the Space Telescope Science Institute, which is operated by the Association of Universities for Research in Astronomy, Inc., under NASA contract NAS 5-26555. These observations are associated with programs #10174, #10494, #10587, #10798, #10886, and #12209.

<sup>2</sup> Department of Physics and Astronomy, The University of Utah, 115 South 1400 East, Salt Lake City, UT 84112, USA (bolton@astro.utah.edu)

<sup>3</sup> Department of Astronomy & Center for Cosmology and Astroparticle Physics, Ohio State University, Columbus, OH 43210, USA

<sup>4</sup> Lawrence Berkeley National Laboratory, Berkeley, CA 94720, USA

<sup>5</sup> Harvard-Smithsonian Center for Astrophysics, 60 Garden St., MS #20, Cambridge, MA 02138, USA

<sup>6</sup> Department of Astronomy, Yale University, New Haven, CT 06520, USA

<sup>7</sup> Department of Physics, Hamilton College, Clinton, NY 13323, USA

<sup>8</sup> Institute of Cosmology and Gravitation, University of Portsmouth, Portsmouth PO1 3FX, UK

<sup>9</sup> Department of Physics and Astronomy, University of California at Irvine, Irvine, CA 92697, USA

<sup>10</sup> Center for Cosmology and Particle Physics, New York University, New York, NY 10003, USA

type galaxies in the local universe (e.g., Gerhard et al. 2001; Cappellari et al. 2006) suffer from mass-profile and orbital-anisotropy degeneracies at cosmological distances where higher-order moments of the line-of-sight velocity profile can no longer be measured reliably.

The phenomenon of strong gravitational lensing permits mass measurements in the central regions of early-type galaxies to the few-percent level. Either on its own (e.g., Warren & Dye 2003; Rusin et al. 2003; Wayth et al. 2005) or in combination with stellar-dynamical constraints (e.g., Treu & Koopmans 2002, 2004; Koopmans & Treu 2003), strong lensing provides the most powerful tool for the measurement of galaxy masses and density distributions across cosmic time. The use of strong lensing for the study of galaxy structure and evolution has historically been constrained by the availability of significant lens samples. By identifying gravitational lens candidates spectroscopically from within the SDSS database, the Sloan Lens ACS (SLACS: Bolton et al. 2006, 2008; Auger et al. 2009) Survey has identified the largest single sample of confirmed strong-lens galaxies, but the small redshift range within the SLACS sample alone limits its utility for the study of galaxy evolution. An initial combination of the SLACS sample with lenses at significantly higher redshift (Koopmans et al. 2006) detected no significant mass-structure evolution, but used a relatively small and heterogeneous higher-redshift sample. Recently, the CFHT Strong Lens Legacy Survey (SL2S: Cabanac et al. 2007; More et al. 2011; Gavazzi et al. 2012) provided a larger sample of strong lenses at higher redshift, which yielded a tentative detection of structural evolution when combined with the SLACS sample (Ruff et al. 2011). The SL2S sample is most fundamentally limited by a lack of source-galaxy redshifts for many systems, compromising the precision with which angular lensing observables can be translated into physical mass constraints.

In this paper, we present a galaxy mass-density profile evolution analysis that combines the SLACS lens sample with lenses recently discovered by the BOSS Emission-Line Lens Survey (BELLS: Brownstein et al. 2012, hereafter Paper I). The BELLS lenses are selected from the BOSS survey with the same spectroscopic selection method employed by SLACS, and are comparable in stellar mass to the SLACS lens galaxies (see §4.2 below.) For both SLACS and BELLS samples, spectroscopic lens and source galaxy redshifts are available for all systems, and SDSS/BOSS spectra provide stellar velocity-dispersion data that may be combined with lensing measurements to constrain the lens-galaxy mass-density profiles.

This paper is organized as follows. Section 2 gives an overview of the observational data that we employ. Section 3 describes our inference methodology and presents our basic evolutionary measurement result. Section 4 presents an investigation of possible systematics and dependences beyond redshift evolution, including those associated with stellar velocity dispersions (§4.1), photometric parameters (§4.2), strong-lensing measurement apertures (§4.3), and lensing selection effects (§4.4). Finally, §5 provides a discussion and conclusions. We assume throughout a general-relativistic FRW cosmology with parameters  $H_0 = 70 \text{ km s}^{-1} \text{ Mpc}^{-1}$ ,  $\Omega_M = 0.3$ , and  $\Omega_\Lambda = 0.7$ , and note that our results are only very weakly sensitive to the exact values of these parameters.

## 2. OBSERVATIONAL SAMPLES

The SLACS and BELLS lenses were selected from imaging and spectroscopic data collected at the 2.5-m SDSS telescope (Gunn et al. 1998, 2006), all of which are included in the public SDSS-III Data Release 9 (Ahn et al. 2012). For the high-resolution imaging follow-up necessary for strong-lensing analysis, all systems in this work were also observed through the F814W (*I*-band) filter using the Wide-Field Channel (WFC) of the Advanced Camera for Surveys (ACS) aboard the *Hubble Space Telescope* (*HST*). For our SLACS data set, we use the 57 early-type grade-A lenses with lensing mass models presented in Bolton et al. (2008). We do not include data for the additional SLACS lenses reported in Auger et al. (2009), since that subset was observed only with the WFPC2, and we wish to maintain as much uniformity as possible. Since the uncertainty in our evolutionary analysis is primarily set by the BELLS sample at the higher redshift end, the omission of these additional SLACS systems has little statistical effect. For our BELLS data set, we use the 22 early-type grade-A lenses presented in Paper I. For all lenses, we use SDSS (for SLACS) and BOSS (for BELLS) spectroscopic data to derive stellar velocity-dispersion likelihood functions. For 6 of our BELLS targets, multiple independent spectroscopic observations are available. We combine the velocity-dispersion likelihood information from these repeat observations in our analysis below.

## 3. BASIC EVOLUTION MEASUREMENT

Following Koopmans et al. (2006, 2009), we constrain the central mass-density profile of the lens galaxies via a Jeans-equation analysis constrained by both strong-lensing aperture masses and stellar kinematics. In this analysis, we model all lenses using a stellar luminosity profile embedded in a *total* mass-density profile (i.e., stars plus dark matter) parameterized as  $\rho \propto r^{-\gamma}$ .

For the parameterization of the luminosity profile, we use the “Nuker” profile described by Lauer et al. (1995), which is a broken power-law with a transition of variable softness between inner and outer regions. We fit the PSF-convolved Nuker profile directly to the *HST I*-band images inside a circular region of radius  $6''$ , and optimize the parameters non-linearly until convergence. This central region is chosen so as to focus on accurately matching the luminosity-profile model to the imaging data over the approximate range of radii probed directly by our lensing and kinematic observables. This approach allows a more accurate Jeans-equation analysis than one based on the globally optimized de Vaucouleurs (1948) models which were used for the measurement of magnitudes and effective radii in Bolton et al. (2008) and Paper I. However, we verify further below that our results do not depend significantly upon our choice of parameterized luminosity-profile form.

Graham et al. (2003) demonstrate that the parameters of the Sérsic (1968) profile are more robust and physically meaningful than those of the Nuker profile for the *global* characterization of galaxy surface-brightness profiles. We emphasize here that the role of the Nuker model in our mass-profile analysis is simply to provide a flexible, convenient, and sufficiently accurate parameterized mathematical model for the luminous tracer distribution

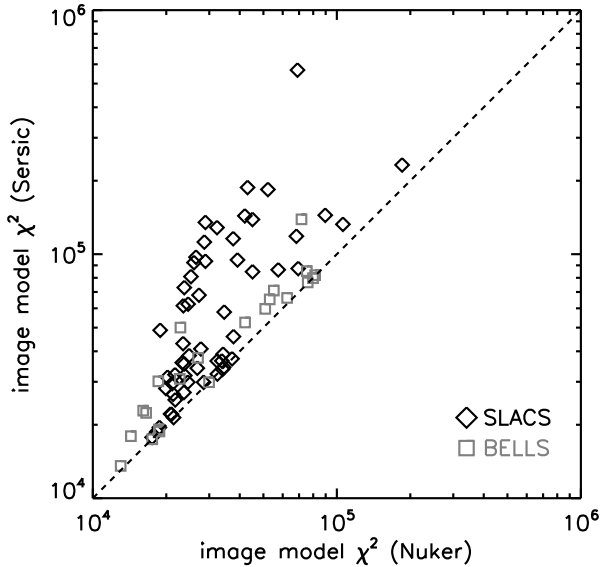


FIG. 1.— Comparison of  $\chi^2$  goodness-of-fit statistics for Sérsic and Nuker parameterized models to SLACS and BELLS lens galaxies used in this work, as fitted within circular regions of radius  $6''$  centered on the lens galaxies.

over the *local* range of radii probed by our strong-lensing and stellar-dynamics observations. We make no physical interpretation of the fitted Nuker model parameters, which were originally conceived to describe the core regions of galaxies. Figure 1 shows a comparison of the  $\chi^2$  goodness-of-fit statistic for Sérsic and Nuker fits to the inner regions of our SLACS and BELLS lens galaxies. The quality of the Nuker fit is as good as or better than that of the Sérsic fit in every case, with the typical improvements in  $\chi^2$  being highly significant.<sup>11</sup> Hence we adopt the Nuker profile as our preferred parameterization within the lensing–dynamical analysis, but we return to the Sérsic model to characterize the distribution of lens-galaxy global profile shapes in §4.2 below.

For each galaxy, we take the measured Einstein radius as a projected aperture-mass constraint on the total mass-density profile. We deproject this mass constraint using the power-law mass model for a gridded range of profile values  $1.1 < \gamma < 2.9$ . Assuming a constant and isotropic velocity-dispersion tensor, we apply the deprojected mass constraint and solve the spherical Jeans equation at each point in the grid of  $\gamma$  values for the radial (squared) velocity-dispersion profile of a tracer population given by the Abel-deprojected luminosity profile for the lens galaxy. We then reproject the luminosity-weighted line-of-sight component of this profile back into two dimensions to predict the line-of-sight velocity dispersion profile across the lens galaxy. The luminosity-weighted squared-dispersion is then integrated over an aperture corresponding to the SDSS ( $3''$  diameter) or BOSS ( $2''$  diameter) spectroscopic fiber aperture blurred by  $1''.8$  FWHM seeing to predict  $\sigma_i(\gamma)$ , the velocity dispersion that would be measured by SDSS or BOSS for lens  $i$  given a logarithmic mass-density slope parameter  $\gamma$ .

<sup>11</sup> See Byun et al. 1996 for a formula expressing the Sérsic profile as a limit of the Nuker profile.

We revisit the method of measurement of the stellar velocity dispersion  $\sigma$  from SDSS and BOSS spectra, in order to (1) ensure the greatest uniformity between the treatment of the SLACS and BELLS samples, (2) maximize the signal-to-noise ratio (S/N) of the BOSS velocity-dispersion measurements by using the full range of spectral data, and (3) propagate the full velocity-dispersion likelihood information in our analysis. This is well motivated since velocity-dispersion uncertainties dominate the statistical error budget, particularly for the lower signal-to-noise ratio (S/N) BOSS spectra. To do this, we develop a new velocity-dispersion measurement code that explicitly projects high-resolution stellar templates through the wavelength-dependent line-spread function recorded on a fiber-by-fiber basis for all BOSS and SDSS spectra. We also derive a new set of stellar templates from the Indo-US library (Valdes et al. 2004), which we furthermore patch (over telluric bands) and extend (to redder and bluer wavelengths) using best-fit model atmospheres selected from the POLLUX database (Palacios et al. 2010). This stellar template generation procedure is described in detail in Bolton et al. (2012), and is used primarily to generate stellar classification templates for use in the BOSS spectroscopic pipeline. For the velocity-dispersion analysis, we only use stars of spectral type A through K. We perform a principal-component analysis decomposition of these templates, and retain the top 5 eigenspectra as our velocity-dispersion template basis. At each trial velocity dispersion, we fit the lens-galaxy spectrum as a linear combination of broadened basis templates (thus marginalizing to some extent over stellar-population uncertainties) plus a quartic polynomial, and accumulate the function  $\chi_i^2(\sigma_i)$  for each lens galaxy  $i$ . We make use of these full  $\chi_i^2(\sigma_i)$  functions, rather than point estimates of velocity dispersion, in our mass-profile analysis. As shown in Shu et al. (2012), this approach allows us to combine data from multiple galaxies and recover unbiased estimates of population distribution parameters even in the limit of low S/N in individual spectra.<sup>12</sup>

To derive our mass-profile constraints, we compose the dynamical information encoded by  $\chi_i^2(\sigma_i)$  with the lensing information encoded by  $\sigma_i(\gamma)$  to obtain the probabilities for the spectroscopic data  $\mathbf{d}_i$  of individual lenses given a value for the logarithmic mass-profile slope  $\gamma$ :

$$p_i(\mathbf{d}_i|\gamma) \propto \exp[-\chi_i^2(\sigma_i(\gamma))/2]. \quad (1)$$

To model the distribution of  $\gamma$  values within the population, we parameterize the conditional probability density function (pdf) of  $\gamma$  at a given lens redshift by a Gaussian whose mean value evolves linearly with redshift:

$$p(\gamma|z; \gamma_0, \gamma_z, s_\gamma) = \frac{1}{\sqrt{2\pi}s_\gamma} \times \exp\left\{-\frac{[\gamma - (\gamma_0 + \gamma_z(z - 0.25))]^2}{2s_\gamma^2}\right\}. \quad (2)$$

Here,  $\gamma_0$  is the mean  $\gamma$  value at redshift  $z = 0.25$ ,  $\gamma_z$

<sup>12</sup> Although we do not use point estimates of velocity dispersion in our analysis, we can quote a median fractional error in velocity dispersion of about 12% and a median absolute error of about  $22 \text{ km s}^{-1}$  for the BELLS lens sample, defined by the half-width of the  $\Delta\chi^2 = 1$  interval about the minimum- $\chi^2$  value.

is the evolution of the mean  $\gamma$  with redshift, and  $s_\gamma$  is the intrinsic scatter in  $\gamma$  at all redshifts. The choice to parameterize the redshift dependence relative to the intermediate value of  $z = 0.25$  is made so as to minimize covariance between the model parameters  $\gamma_0$  and  $\gamma_z$ .

With these ingredients, we can now express the probability of the observed spectroscopic data for lens galaxy  $i$  given the evolution-relation parameters as

$$p(\mathbf{d}_i|\gamma_0, \gamma_z, s_\gamma) = \int d\gamma p_i(\mathbf{d}_i|\gamma)p(\gamma|z_i; \gamma_0, \gamma_z, s_\gamma), \quad (3)$$

with the two factors in the integral given by Equations 1 and 2. Finally, the likelihood function for the population parameters is obtained from the product over all lens galaxies in the sample:

$$\begin{aligned} \mathcal{L}(\gamma_0, \gamma_z, s_\gamma|\{\mathbf{d}_i\}) &= p(\{\mathbf{d}_i\}|\gamma_0, \gamma_z, s_\gamma) \\ &= \prod_i p(\mathbf{d}_i|\gamma_0, \gamma_z, s_\gamma), \end{aligned} \quad (4)$$

with the individual factors obtained from Equation 3. We grid the space of  $(\gamma_0, \gamma_z, s_\gamma)$  and calculate Equation 4 at each grid point, thereby mapping out the likelihood surface for our evolution-relation parameters. We assume a prior  $p(\gamma_0, \gamma_z, s_\gamma)$  that is uniform in  $\gamma_0$ ,  $\gamma_z$ , and  $\log s_\gamma$  to define the posterior probability

$$p(\gamma_0, \gamma_z, s_\gamma|\{\mathbf{d}_i\}) \propto \mathcal{L}(\gamma_0, \gamma_z, s_\gamma|\{\mathbf{d}_i\})p(\gamma_0, \gamma_z, s_\gamma). \quad (5)$$

Figure 2 shows maximum-likelihood estimates of  $\gamma$  for the individual lenses (for illustrative purposes), as well as the posterior probability contours for the zero-point  $\gamma_0$  and evolution  $\gamma_z$  of the population mean mass-density slope for both the Nuker profile-based calculation and the alternative de Vaucouleurs profile-based calculation. Characterizing the one-dimensional measurements via marginalization and Gaussian fitting, we find  $\gamma_z = -0.60 \pm 0.15$ ,  $\gamma_0 = 2.11 \pm 0.02$ , and  $\log_{10}(s_\gamma) = \log_{10}(0.14) \pm 0.06$  dex. Thus, we find a slightly super-isothermal average profile (as in Koopmans et al. 2009 and Auger et al. 2010), and a very significant signal of evolution in the total mass-density profile of strong-lens galaxies in the sense of a ‘‘steeper’’ (more centrally concentrated) profile with increasing cosmic time (decreasing redshift).

To verify the robustness of our result against changes in the details of our analysis procedure, we run the same mass-profile evolution calculation using the best-fit de Vaucouleurs models to describe the luminosity profiles of the lens galaxies, and also using Nuker models fitted to the *HST* imaging data with flat rather than noise-based pixel weighting. The resulting parameters and associated uncertainties for these alternate calculations are given in Table 1, and show only insignificant differences with respect to our reference model results. We also verify the degree of information added by the BELLS sample by repeating the mass-density profile evolution analysis using the SLACS sample alone. This computation yields a value for the evolution of the mean logarithmic mass-density profile slope of  $\gamma_z = -0.61 \pm 0.26$ : consistent with the SLACS+BELLS result, but at much lower significance given the reduced redshift baseline. The other parameters of this SLACS-only analysis are also listed in Table 1.

#### 4. INVESTIGATING NON-EVOLUTIONARY EFFECTS

Before discussing our basic result further, we explore whether the mass-density profile redshift dependence that we measure could reflect the signature of some other physical dependence that is introduced through systematic differences between the higher-redshift (BELLS) and lower-redshift (SLACS) components of our sample. For reference, Figure 3 shows the variation of multiple other parameters with redshift within the combined SLACS+BELLS lens sample that is used in this work.

##### 4.1. Velocity-dispersion effects

The first alternative that we examine is a systematic variation of the typical sample velocity dispersion with redshift. Since the statistical velocity-dispersion uncertainties and the mass-profile uncertainties are almost perfectly correlated, we do not attempt to fit and interpret  $\gamma$  versus  $\sigma$ , but rather we examine the variation of  $\sigma$  with redshift. First, we correct the  $\chi^2(\sigma)$  velocity-dispersion baselines from the observational aperture velocity dispersion  $\sigma$  for each lens  $i$  to the estimated value  $\sigma_e$  within an aperture of one effective radius, using the empirical formula of Cappellari et al. (2006):

$$\sigma_{e,i} = (R_{\text{obs}}/R_e)^{0.06} \sigma_i, \quad (6)$$

where  $R_{\text{obs}} = 1''.5$  for SDSS and  $1''.0$  for BOSS. The applied correction  $(R_{\text{obs}}/R_e)^{0.06} - 1$  within the sample has a (signed) median of  $-1\%$  and an RMS absolute value of  $3\%$ , since the effective radii of the lenses are generally comparable to the angular radius subtended by the spectroscopic fiber. Although the correction relation is derived from galaxies in the local universe, the corrections are small enough that we assume any higher-order redshift-dependent effects to be most likely negligible.

We fit for the distribution of  $\sigma_e$  values within the sample as a function of redshift using the same method as for the  $\gamma$  distribution above. We consider an evolving log-normal model for the population distribution in analogy to Equation 2 as follows:

$$\begin{aligned} p(\log_{10} \sigma_e|z; m_0, m_z, s_\sigma) &= \frac{1}{\sqrt{2\pi}s_\sigma} \\ &\times \exp\left\{-\frac{[\log_{10} \sigma_e - (m_0 + m_z(z - 0.25))]^2}{2s_\sigma^2}\right\}, \end{aligned} \quad (7)$$

for  $\sigma_e$  in  $\text{km s}^{-1}$ . Our notation follows Shu et al. (2012) in using  $m$  to denote the peak in the population pdf of  $\log_{10} \sigma_e$  values, with  $m_0$  representing the value at  $z = 0.25$  and  $m_z$  parameterizing its evolution with redshift. We constrain the parameters of this model as described via Equations 1–5 above, using  $\chi_i^2(\sigma_e)$  instead of  $\chi_i^2(\sigma_i(\gamma))$ . We find best-fit values of  $m_0 = 2.39 \pm 0.01$ ,  $m_z = -0.033 \pm 0.053$ , and  $\log_{10} s_\sigma = \log_{10}(0.06) \pm 0.04$  dex. Hence, we find no significant evidence of evolution in the mean value of the distribution of  $\sigma_e$  values within our sample of lenses.

The upper left panel of Figure 3 shows the maximum-likelihood  $\sigma_e$  estimates for the SLACS and BELLS early-type lens galaxies as a function of redshift, along with the best-fit evolution relation and intrinsic scatter. While there is no significant evolution overall, we do see several possible outliers. To gauge the effect of these outliers on our  $\gamma$  evolution analysis, we re-do our mass-profile

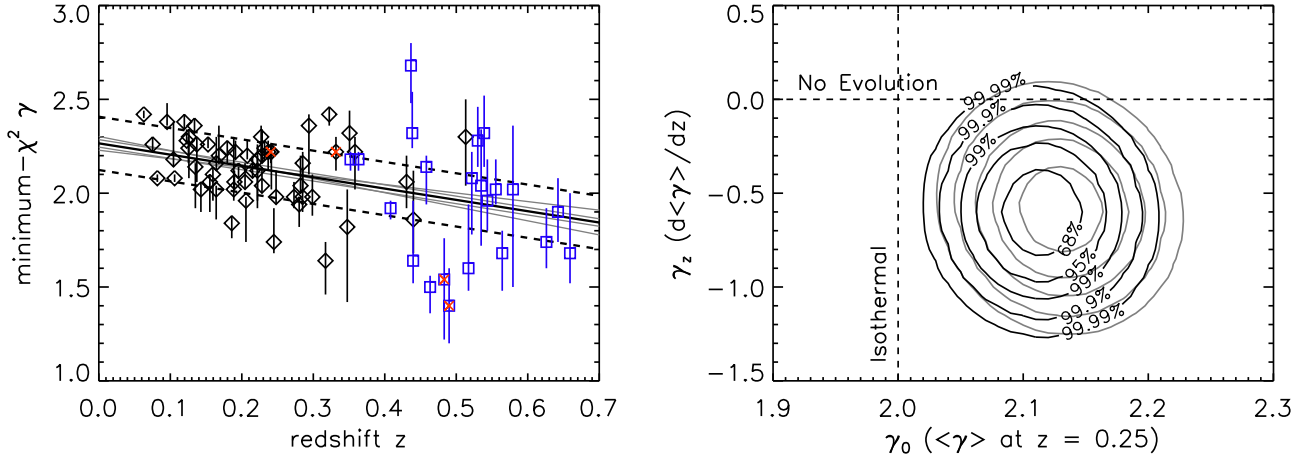


FIG. 2.— *Left*: Minimum- $\chi^2$  values for the logarithmic total mass-density profile slope  $\gamma$  for SLACS (black diamonds) and BELLS (blue squares) lenses. Error bars indicate  $\Delta\chi^2 = 1$ . The solid line shows the best-fit relation, gray lines indicate the “1-sigma” error in the slope and zero-point of this relation, and dashed lines indicate the best-fit intrinsic RMS population scatter. Red crosses indicate systems with a maximum-likelihood log-velocity dispersion ( $\log_{10} \sigma_e$ , in  $\text{km s}^{-1}$ ) either greater than 2.5 or less than 2.2 (see Figure 3.) Data points and error bars are for illustrative purposes only: the population parameter fits are done using the full  $\chi^2(\gamma)$  function for each lens, as described in §3. *Right*: Posterior probability contours enclosing credible regions for the zero-point and evolution of the logarithmic mass-density slope parameter  $\gamma$ . Black curves are for the Nuker profile-based analysis; gray curves are for a de Vaucouleurs profile-based analysis.

TABLE 1  
MASS-PROFILE EVOLUTION PARAMETERS UNDER VARIOUS FITTING SCENARIOS

Subset	$\gamma_0$	$\gamma_z$	$\log_{10} \sigma_\gamma$
All, statistical pixel weight	$2.11 \pm 0.02$	$-0.60 \pm 0.15$	$\log_{10}(0.14) \pm 0.06$ dex
All, flat pixel weight	$2.12 \pm 0.02$	$-0.61 \pm 0.15$	$\log_{10}(0.14) \pm 0.05$ dex
De Vaucouleurs image model	$2.13 \pm 0.02$	$-0.58 \pm 0.15$	$\log_{10}(0.15) \pm 0.05$ dex
SLACS lenses only	$2.11 \pm 0.02$	$-0.61 \pm 0.26$	$\log_{10}(0.13) \pm 0.06$ dex
Velocity-dispersion errors < 15%	$2.12 \pm 0.02$	$-0.58 \pm 0.15$	$\log_{10}(0.14) \pm 0.06$ dex
$2.2 < \log_{10} \sigma(\text{km s}^{-1}) < 2.5$	$2.11 \pm 0.02$	$-0.58 \pm 0.15$	$\log_{10}(0.14) \pm 0.06$ dex

evolution computation excluding the four lenses whose maximum-likelihood  $\log_{10} \sigma_e$  estimates (in  $\text{km s}^{-1}$ ) are either less than 2.2 or greater than 2.5 (corresponding to  $158 \text{ km s}^{-1}$  and  $316 \text{ km s}^{-1}$  respectively). In this case, we find a value for the evolution of the population mean  $\gamma$  of  $\gamma_z = -0.58 \pm 0.15$ , which differs only insignificantly from the value we find when including all lenses. Table 1 contains the full parameter set from this fit.

Changes in the redshift and spectroscopic S/N of the spectra from which the velocity-dispersions are measured are not likely to contribute to our observed signal. If such effects were driving our evolutionary measurement, we would expect to see them reflected in a significant apparent evolution in the velocity-dispersion distribution of our combined sample with redshift. However, as shown above, we do not see this effect to any significant degree. Furthermore, the hierarchical likelihood-stacking method that we use for incorporating velocity-dispersion information into our current population analysis has been tested and verified in Shu et al. (2012). Specifically, that work has shown that increasing the redshift and simultaneously decreasing the S/N of the spectra used for kinematic analysis does not introduce any bias into the estimated parameters of the population velocity-dispersion function estimated from multiple spectra. If we exclude the 4 out of 79 lenses within our sample whose esti-

mated velocity-dispersion errors are in excess of 15% of their maximum-likelihood velocity-dispersion values, we obtain  $\gamma_z = -0.58 \pm 0.15$ , which again differs only insignificantly from the value we find when including all lenses. Table 1 reports all parameters from this fit.

#### 4.2. Photometric parameter dependence

From Figure 3, we see no significant overall redshift variation in the combined sample in either mean stellar mass  $M_*$ , mean effective radius  $R_e$ , or mean Sérsic index  $n$ . The lack of an apparent stellar-mass trend can be considered in terms of the luminosity-function evolution results of Wake et al. (2006), which show no significant evolution in the number density of massive elliptical galaxies from redshift  $z \simeq 0.6$  to the present epoch, once passive stellar evolution is taken into account. This suggests that we are probing a similar range of galaxies across the redshift range spanned by our lens sample. The lack of a detected trend in effective radius is also consistent with the modest size evolution seen for massive elliptical galaxies at lower redshifts (e.g., van der Wel et al. 2008), again suggesting that our sample represents a broadly similar population of galaxies across redshift. Of course, the question of merging complicates the identification of corresponding galaxy populations across redshift, and we will return to this issue in §5.

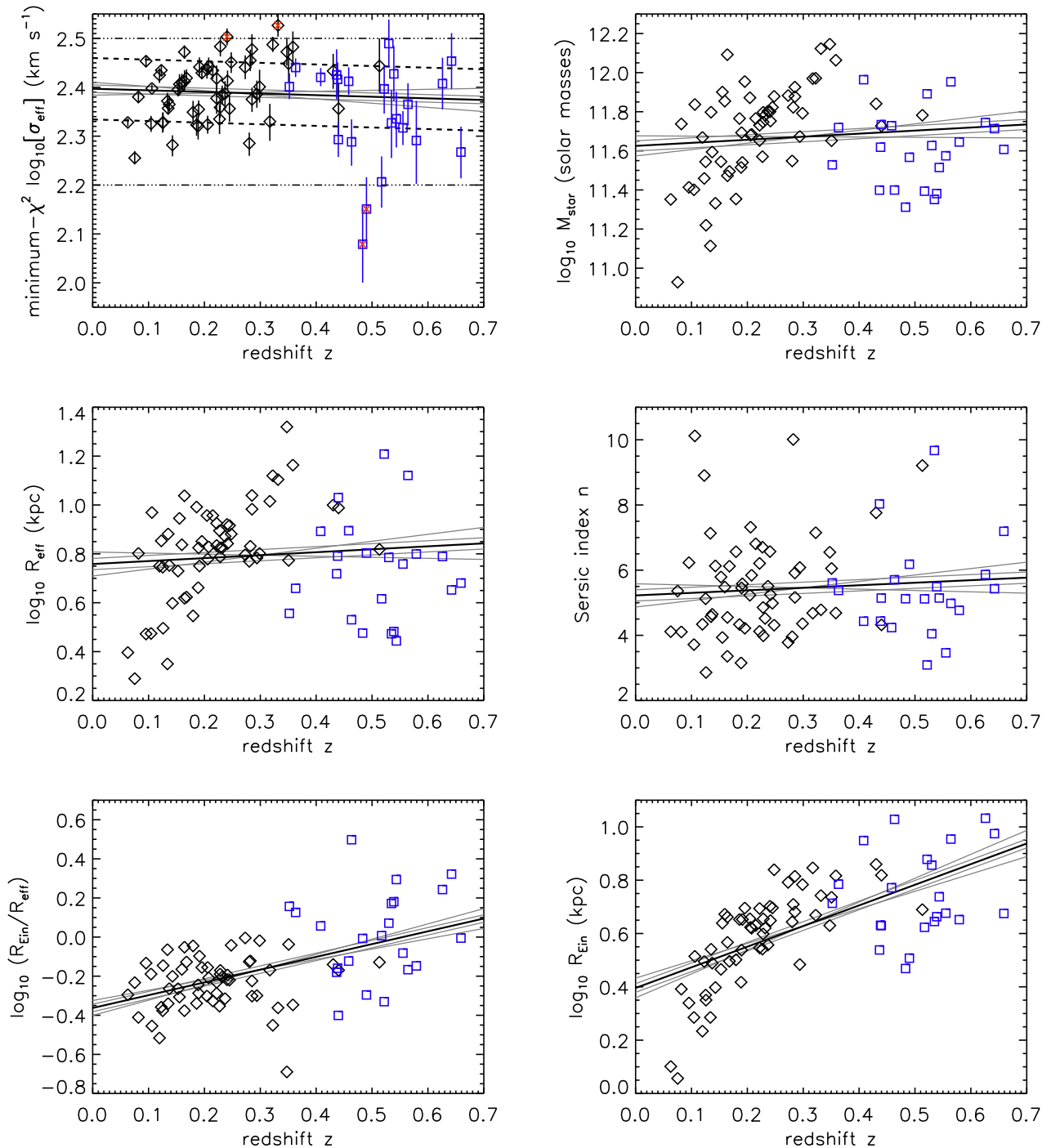


FIG. 3.— Redshift variation of other observable quantities in the sample of 79 early-type SLACS (black diamonds) and BELLS (blue squares) lens galaxies. From upper left to lower right, these are: stellar velocity dispersion within one effective radius, estimated stellar mass, effective radius, Sérsic index, ratio of lensing Einstein radius to lens-galaxy effective radius, and Einstein radius in kiloparsecs at the redshift of the lens galaxy. The solid black line shows the best-fit relation, and gray lines indicate the “1-sigma” error in the slope and zero-point of this relation. For all plots except the velocity-dispersion plot, the fit errors have been estimated via bootstrap resampling. For the velocity-dispersion plot, values have been scaled from the observational aperture (SDSS or BOSS) to one effective radius using the empirical relation of Cappellari et al. (2006), error bars indicate  $\Delta\chi^2 = 1$ , and dashed lines indicate the best-fit intrinsic RMS population scatter. Dot-dashed lines bound the region  $2.2 < \log_{10} \sigma_e < 2.5$ , and lenses with maximum-likelihood values outside this range are marked with red crosses. The velocity-dispersion evolution fit is done using the full  $\chi^2(\sigma_e)$  function for each galaxy, as described in the text.

We may also address the issue of heterogeneous sizes, stellar masses, and Sérsic indices in our sample head-on, by introducing them as second independent variables along with redshift in our fit for the dependence of the mass-profile parameter  $\gamma$ , since (in contrast to the errors on velocity dispersion) the *statistical* errors on  $M_*$ ,  $R_e$ , and  $n$  are very small, and much more uncorrelated with the dominant uncertainty in  $\gamma$ . For these second-independent-variable analyses, we use *HST* *I*-band de Vaucouleurs model magnitudes and effective radii from Bolton et al. (2008) and Paper I. Sérsic indices are obtained by fitting two-dimensional PSF-convolved elliptical Sérsic models to the same image data as used for the de Vaucouleurs photometry in those works, covering a  $51'' \times 51''$  square region centered on the lens galaxies. Our stellar mass estimates are obtained by scaling the passively-evolving stellar-population model of Maraston et al. (2009) to the observed and Galactic extinction-corrected *I*-band magnitudes.

We consider bi-variate population models of the form

$$p(\gamma|z, x; \gamma_0, \gamma_z, \gamma_x, s_\gamma) = \frac{1}{\sqrt{2\pi}s_\gamma} \times \exp\left\{-\left[\gamma - (\gamma_0 + \gamma_z(z - 0.25) + \gamma_x(x - c_x))\right]^2 / (2s_\gamma^2)\right\}, \quad (8)$$

where  $x = \log_{10}(M_*/M_\odot)$ ,  $\log_{10}(R_e/1 \text{ kpc})$ , or  $\log_{10}(n)$  depending upon the second independent variable under consideration, with the constant  $c_x = 11.7$ ,  $0.7$ , and  $0.7$  for the three cases respectively. We grid the four-dimensional parameter spaces for these three cases in order to map out likelihoods and posterior probabilities, and show the results for the joint dependence parameters in Figure 4. In all three cases, the dependence of  $\gamma$  on redshift is more significant than the dependence on the second variable. We evaluate the statistical improvements represented by these various two-variable models over the redshift-only model via the likelihood ratio test, expressed by the following  $\Delta\chi^2$  statistic:

$$\Delta\chi_x^2 = 2 \ln \left\{ \max [\mathcal{L}(\gamma_0, \gamma_z, \gamma_x, s_\gamma | \{\mathbf{d}_i\})] \right\} - 2 \ln \left\{ \max [\mathcal{L}(\gamma_0, \gamma_z, s_\gamma | \{\mathbf{d}_i\})] \right\}. \quad (9)$$

The greatest improvement comes from the introduction of stellar mass as a second independent variable, for which  $\Delta\chi_x^2 = 5.07$ . The introduction of effective radius as a second dependent variable gives a fairly comparable  $\Delta\chi_x^2 = 4.65$ , while the introduction of dependence upon Sérsic index gives a relatively insignificant  $\Delta\chi_x^2 = 1.82$ . Motivated by the evidence for stellar-mass dependence, we also compare a model with dependence on stellar mass alone to the initial model with dependence on redshift alone, and find the redshift-dependence model preferred by  $\Delta\chi^2 = 7.16$ . We note also that our stellar mass estimates are subject to much greater systematic uncertainty than our redshift estimates. To summarize, we see some evidence for shallower profiles in larger and/or more massive galaxies, but this cannot explain the evolutionary signal that we detect.

#### 4.3. Lensing aperture effects

Figure 3 shows a non-negligible trend of increase with redshift in the Einstein radius, both in absolute units and relative to the effective radii of the lens galaxies. This trend is chiefly a consequence of the cosmic geometry

of strong lensing for increasing lens redshifts: to leading order, a given galaxy has a characteristic angular scale for strong lensing that does not diminish with increasing redshift, whereas the apparent angular scale of a given physical length unit does diminish with increasing redshift. Although the Einstein radius in kiloparsecs does not represent a physical property of the lens galaxy, we must consider the possibility that this variation of *physical* Einstein radius with redshift impacts our mass-profile evolution measurement. If we assume as an alternative hypothesis that lens galaxies do not evolve structurally, our apparent evolution result must imply that the average mass-density profile is *shallower* with increasing radii out from the center of the galaxy. At face value, this would be at variance with both a de Vaucouleurs or Sérsic stellar profile and a Navarro et al. (1996) dark-matter profile, since both profiles become *steeper* at increasing radii. An intriguing possibility is that we might be seeing direct evidence for an inflection zone between the stellar-dominated inner regions and the halo-dominated outer regions of our lens galaxies, which in certain combined baryon+halo models can exhibit a localized trend towards a shallower profile with increasing radius (see, e.g., Figure 8 of Gavazzi et al. 2007). However, it should be noted that our lensing+dynamics analysis constrains an average density profile interior to the Einstein radius, rather than a boundary value at the Einstein radius, so this interpretation is not straightforward. The most direct means of addressing this question further would be through spatially resolved stellar kinematics of the SLACS and BELLS lenses, which in combination with the strong-lensing mass normalizations could test the redshift and aperture dependences separately.

Contributions from large-scale structure fluctuations along the line of sight (i.e., beyond the host dark-matter halo scale of the lens galaxies) will not contribute significantly to our results. The influence of large-scale structure variance will increase with the redshift of the *lensed background galaxy*  $z_{\text{BG}}$ , and hence the contribution of this effect in SLACS and BELLS lenses with source redshifts  $z_{\text{BG}} \lesssim 1.0$  will be significantly smaller than for lensed quasars or cluster-lensed giant arcs at higher redshifts. Large-scale structure fluctuations in the lensing convergence  $\kappa$  (projected surface density scaled to the critical density for lensing: e.g., Narayan & Bartelmann 1996) are expected to be below the 1% level over this redshift range (e.g., Dalal et al. 2005). Hence these fluctuations are sub-dominant to the lensing Einstein measurement errors, which are in turn subdominant to velocity-dispersion uncertainties. In addition, since these will be fluctuations about the mean density, they are a source of noise rather than bias in our measurement, and will average out with increasing sample size.

#### 4.4. Spectroscopic and lensing selection effects

Arnesen et al. (2012) have quantified the combined bias effects of spectroscopic candidate selection and strong-lens confirmation as a function of mass-density profile parameters for lens surveys with the characteristics of SLACS and BELLS, using detailed Monte Carlo simulations. The SLACS and BELLS simulations are distinguished primarily by differences in spectroscopic emission-line detection depth (BELLS coming from deeper BOSS data), background-galaxy red-

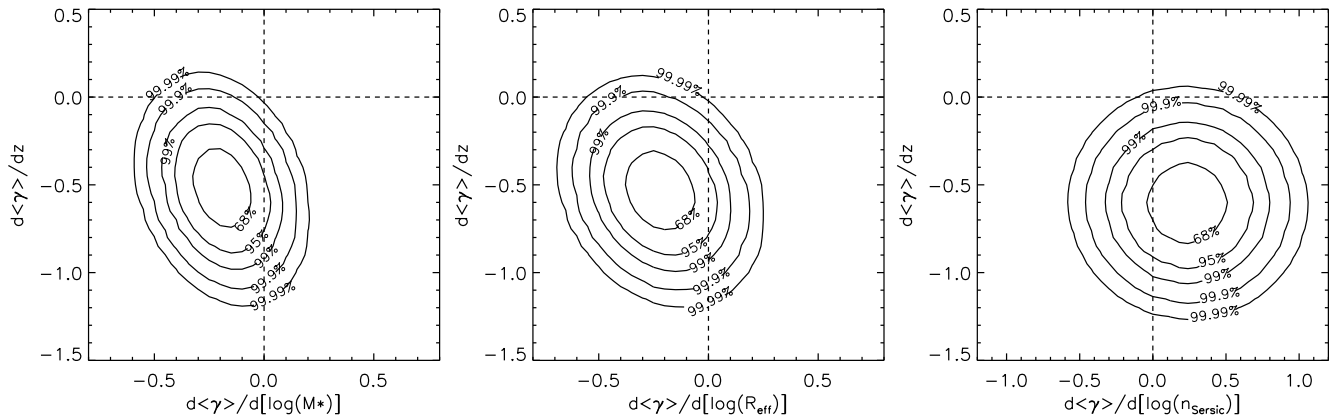


FIG. 4.— Posterior probability contours enclosing credible regions for the joint dependence of the population mean logarithmic mass profile slope  $\gamma$  on: redshift and stellar mass (*left*); redshift and effective radius (*center*); and redshift and Sérsic index (*right*). Stellar masses are estimated by scaling passively evolving Maraston et al. (2009) models to the observed *HST* F814W magnitudes. Dashed lines indicate the lines of no dependence of the population mean  $\gamma$  value on redshift (horizontal) or on the various second independent variables (vertical). Zero-point and intrinsic population scatter parameters have been marginalized in all cases.

shift (BELLS being higher on average), and spectroscopic fiber size (BELLS having the 2''-diameter BOSS fiber, SLACS having the 3''-diameter SDSS fiber). Figure 5 of that work presents the relative selection and confirmation probabilities for lenses as a function of angular Einstein radius  $\theta_E$  and mass-profile slope  $\gamma$  for both SLACS-like and BELLS-like surveys. The  $\theta_E$  dependence incorporates the dependence on velocity dispersion, lens redshift, and source redshift in the particular scaled angular combination that is directly relevant for strong lensing. We use the data from this work to determine the magnitude of any possible lensing selection bias in our mass-profile evolution measurement.

For each lens in our sample, we select all simulated systems from the Arneson et al. (2012) data that are within  $\pm 0.1$  dex in  $\theta_E$  of that lens's  $\theta_E$  value, and that meet the simulated criteria of being both spectroscopically selected *and* modelable as strong lenses. Since the parent population of simulated lenses is distributed uniformly in  $\gamma$  from 1 to 3 (the full range of mathematically allowable values), the histogram of these selected subsets defines the relative probability of a simulated lens appearing in our observational sample as a function of  $\gamma$ . We then assume an intrinsic distribution of  $\gamma$  values given by the best-fit population parameters from §3 above, evaluated for the redshift of the real lens under consideration. We weight this intrinsic distribution by the  $\gamma$ -dependent selection probability, and compute the mean  $\gamma$  value over the selected subset of simulated lenses with this combined weighting. Finally, we subtract off the intrinsic mean  $\gamma$  value to determine the expected bias in  $\gamma$  for the real lens under consideration. Figure 5 shows the results of this calculation for all lenses in our observational sample. The expected selection bias in  $\gamma$  is at the level of  $\sim 0.01$ , well below the evolution signal that we detect, and shows no significant redshift dependence or variation between the SLACS and BELLS samples.

## 5. DISCUSSION AND CONCLUSIONS

Comparing our mass-profile evolution result to that of Ruff et al. (2011), we find that our best value for  $\gamma_z$  is more than twice as large. However, the significance of the discrepancy, given the combined uncertainties in

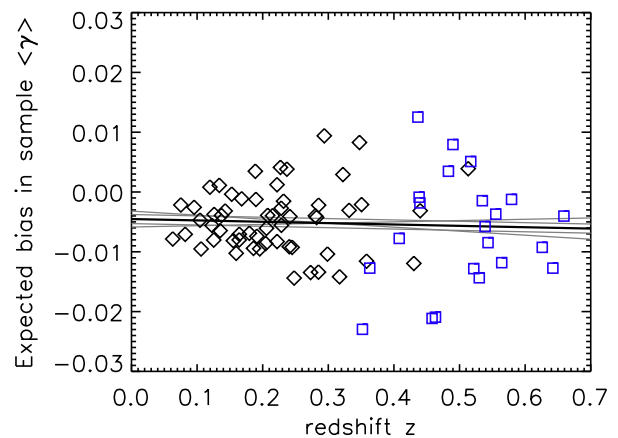


FIG. 5.— Expected mass-profile parameter biases for SLACS (black diamond) and BELLS (blue square) lenses, based on combined spectroscopic selection and lens confirmation biases as simulated by Arneson et al. (2012).

both measurements, is less than 2-sigma. Furthermore, we note that the magnitude of the mass-profile evolution detected in this work, although expressed per unit redshift, is detected over a redshift interval less than one.<sup>13</sup> The Ruff et al. (2011) analysis includes lens systems out to redshift  $z \approx 1$  from the Lenses Structure and Dynamics Survey (LSD: e.g., Treu & Koopmans 2002, 2004; Koopmans & Treu 2003). Hence if the bulk of evolution is concentrated towards the more recent half of the interval since redshift unity (which encompasses 65% of the cosmic time elapsed), the two results would be brought into further agreement. We also note that our result is consistent with the lack of significant evolution found in Koopmans et al. (2006) given the uncertainties in that work. Finally, we note that the tension between the two measurements is somewhat lessened by the possibility of an additional mode of variation of  $\gamma$  with lens-galaxy mass and/or size.

<sup>13</sup>  $\Delta z \approx 0.6$  measured from the minimum SLACS lens redshift of 0.06 to the maximum BELLS lens redshift of 0.66, or  $\Delta z \approx 0.3$  measured from the median SLACS redshift of 0.2 to the median BELLS redshift of 0.5.

One possible explanation for evolution towards steeper mass profiles with cosmic time could be an ongoing contribution from dissipative processes, as suggested by Ruff et al. (2011). However, baryonic dissipation sufficient to significantly modify the global mass-density structure would necessarily be accompanied by appreciable star-formation, which is at variance with the uniformly old stellar populations that are characteristic of massive early-type galaxies (e.g., Thomas et al. 2005; Maraston et al. 2009). An alternative possibility is that hierarchical dry-merging processes can lead to an evolution in the inner mass-density profile. Cosmological simulations of the formation and assembly of galaxies suggest that massive ( $M_* > 10^{11} M_\odot$ ) ellipticals will typically have assembled only half of their  $z = 0$  stellar mass at a redshift of  $z = 0.8$  (De Lucia et al. 2006). On smaller-scales that resolve the density structure within galaxies, both analytic work (Dehnen 2005) and numerical studies (Fulton & Barnes 2001; Kazantzidis et al. 2006) find that halo core profiles are preserved under major merging. However, in the simulations of Nipoti et al. (2009), which focused on strong-lensing observables in the evolution of the central mass-density profile under the merging of isothermal progenitors, the specific channel of *off-axis major mergers* produces a systematic evolution towards steeper-than-isothermal remnant profiles, with a magnitude comparable to the integrated evolution seen here in our SLACS+BELLS lens sample. A possible scenario that emerges is hence one in which the evolution in the distribution of stellar tracers (and hence in the observed mass-size relation) in massive early-type galaxies is driven primarily by minor dry mergers (e.g., Naab et al. 2009; Hopkins et al. 2009; van Dokkum et al. 2010) at higher redshifts, while an evolution in their total mass-density structure is driven by major dry mergers at lower redshifts, with off-axis merger configurations playing the most important role. An alternative explanation could be an evolution to a higher fraction of satellite (relative to central) galaxies at lower redshifts (e.g., Wake et al. 2008; Wetzel & White 2010), with consequently increased central mass concentrations from the effects of tidal stripping.

When galaxy mergers are considered, the question of matching present-day galaxies with their population progenitors at higher redshift becomes more complicated. Our result should therefore be regarded as a constraint on the recent structural evolution of galaxies within the approximate range  $10^{11} < M_*/M_\odot < 10^{12}$ , with the understanding that if major galaxy mergers are a significant driver of that evolution, the identity of a given galaxy is not fixed by its stellar mass even in the absence of star formation. A single major dry merger with a 1:1 mass ratio will place the product galaxy 0.3 dex higher in stellar mass than its two progenitor galaxies, which represents a relatively modest change compared to the range of masses spanned by galaxies in the universe. If we furthermore assume that similar physical processes are at work for galaxies just beyond the reach of our sample in stellar mass, we can be confident that our analysis is generally applicable to the structural evolution of massive galaxies. With more detailed observations, a more controlled sample, and a tighter quantitative connection to galaxy merger simulations, we can make our current result more precise as to the implied rate and nature of

mergers.

We have many avenues to expand our observational study of the density-structure evolution of massive elliptical galaxies using the combined SLACS and BELLS samples. First, we will pursue an analysis based upon more physically motivated star-plus-halo models of the lens galaxies (see, e.g., Jiang & Kochanek 2007), rather than the somewhat *ad hoc* class of power-law models considered here. Second, we will pursue deeper ground-based spectroscopy of the BELLS lens sample, since the BELLS velocity-dispersion uncertainties are the dominant limitation to the statistical precision of our current result. Third, deep and high-resolution multi-band imaging of BELLS lenses can be obtained, since currently our only multi-band imaging data for the BELLS lenses is from the SDSS, and is affected by large photometric errors and background-galaxy flux confusion. These deeper data can be used to model the lens-galaxy stellar populations in greater detail, and to determine stellar masses that are more accurate than the simple luminosity-scaling estimates that we have adopted in this paper. Better stellar-mass estimates would also allow for a meaningful separation of the stellar and dark-matter contributions to the total lensing mass. Fourth, we can incorporate mass-profile constraining information from the resolved lensed images in addition to stellar dynamics. Finally, the availability of new BELLS lens candidates from continuing BOSS observations should lead to a ten-fold increase in the sample of lenses at higher redshift, allowing us to more robustly measure the joint dependence of early-type galaxy structure on the two independent variables of mass and redshift.

ASB and JRB acknowledge the hospitality of the Max-Planck-Institut für Astronomie, where a portion of this work was completed. CSK is supported by NSF grant AST-1009756. The authors thank the anonymous referee for constructive comments and suggestions that led to substantial improvements in this work.

Funding for SDSS-III has been provided by the Alfred P. Sloan Foundation, the Participating Institutions, the National Science Foundation, and the U.S. Department of Energy Office of Science. The SDSS-III web site is <http://www.sdss3.org/>. SDSS-III is managed by the Astrophysical Research Consortium for the Participating Institutions of the SDSS-III Collaboration including the University of Arizona, the Brazilian Participation Group, Brookhaven National Laboratory, University of Cambridge, University of Florida, the French Participation Group, the German Participation Group, the Instituto de Astrofísica de Canarias, the Michigan State/Notre Dame/JINA Participation Group, Johns Hopkins University, Lawrence Berkeley National Laboratory, Max Planck Institute for Astrophysics, New Mexico State University, New York University, Ohio State University, Pennsylvania State University, University of Portsmouth, Princeton University, the Spanish Participation Group, University of Tokyo, The University of Utah, Vanderbilt University, University of Virginia, University of Washington, and Yale University.

Support for *HST* programs #10174, #10494, #10587, #10798, #10886, and #12209 was provided by NASA through a grant from the Space Telescope Science Insti-

tute, which is operated by the Association of Universities for Research in Astronomy, Inc., under NASA contract NAS 5-26555.

## REFERENCES

- Ahn, C. P., et al. 2012, ApJS, submitted (arXiv:1207.7137)  
 Arneson, R. A., Brownstein, J. R., & Bolton, A. S. 2012, ApJ, 753, 4  
 Auger, M. W., et al. 2009, ApJ, 705, 1099  
 —. 2010, ApJ, 724, 511  
 Bell, E. F., et al. 2006, ApJ, 640, 241  
 Bolton, A. S., Burles, S., Koopmans, L. V. E., Treu, T., & Moustakas, L. A. 2006, ApJ, 638, 703  
 Bolton, A. S., et al. 2008, ApJ, 682, 964  
 —. 2012, AJ, submitted (arXiv:1207.7326)  
 Brownstein, J. R., et al. 2012, ApJ, 744, 41  
 Byun, Y.-I., et al. 1996, AJ, 111, 1889  
 Cabanac, R. A., et al. 2007, A&A, 461, 813  
 Cappellari, M., et al. 2006, MNRAS, 366, 1126  
 Cole, S., Lacey, C. G., Baugh, C. M., & Frenk, C. S. 2000, MNRAS, 319, 168  
 Conroy, C., Gunn, J. E., & White, M. 2009, ApJ, 699, 486  
 Daddi, E., et al. 2005, ApJ, 626, 680  
 Dalal, N., Hennawi, J. F., & Bode, P. 2005, ApJ, 622, 99  
 Dawson, K. S., et al. 2012, AJ, submitted (arXiv:1208.0022)  
 De Lucia, G., Springel, V., White, S. D. M., Croton, D., & Kauffmann, G. 2006, MNRAS, 366, 499  
 de Vaucouleurs, G. 1948, Annales d'Astrophysique, 11, 247  
 Dehnen, W. 2005, MNRAS, 360, 892  
 Eisenstein, D. J., et al. 2001, AJ, 122, 2267  
 —. 2005, ApJ, 633, 560  
 —. 2011, AJ, 142, 72  
 Fulton, E., & Barnes, J. E. 2001, Ap&SS, 276, 851  
 Gavazzi, R., Treu, T., Marshall, P. J., Brault, F., & Ruff, A. 2012, arXiv:1202.3852  
 Gavazzi, R., Treu, T., Rhodes, J. D., Koopmans, L. V. E., Bolton, A. S., Burles, S., Massey, R. J., & Moustakas, L. A. 2007, ApJ, 667, 176  
 Gerhard, O., Kronawitter, A., Saglia, R. P., & Bender, R. 2001, AJ, 121, 1936  
 Graham, A. W., Erwin, P., Trujillo, I., & Asensio Ramos, A. 2003, AJ, 125, 2951  
 Gunn, J. E., et al. 1998, AJ, 116, 3040  
 —. 2006, AJ, 131, 2332  
 Hopkins, P. F., Bundy, K., Murray, N., Quataert, E., Lauer, T. R., & Ma, C.-P. 2009, MNRAS, 398, 898  
 Jiang, G., & Kochanek, C. S. 2007, ApJ, 671, 1568  
 Kauffmann, G., White, S. D. M., & Guiderdoni, B. 1993, MNRAS, 264, 201  
 Kazantzidis, S., Zentner, A. R., & Kravtsov, A. V. 2006, ApJ, 641, 647  
 Khochfar, S., & Burkert, A. 2003, ApJ, 597, L117  
 Koopmans, L. V. E., & Treu, T. 2003, ApJ, 583, 606  
 Koopmans, L. V. E., Treu, T., Bolton, A. S., Burles, S., & Moustakas, L. A. 2006, ApJ, 649, 599  
 Koopmans, L. V. E., et al. 2009, ApJ, 703, L51  
 Lauer, T. R., et al. 1995, AJ, 110, 2622  
 Maraston, C., Strömbäck, G., Thomas, D., Wake, D. A., & Nichol, R. C. 2009, MNRAS, 394, L107  
 More, A., Cabanac, R., More, S., Alard, C., Limousin, M., Kneib, J.-P., Gavazzi, R., & Motta, V. 2011, ArXiv e-prints  
 Naab, T., Johansson, P. H., & Ostriker, J. P. 2009, ApJ, 699, L178  
 Narayan, R., & Bartelmann, M. 1996, ArXiv Astrophysics e-prints  
 Navarro, J. F., Frenk, C. S., & White, S. D. M. 1996, ApJ, 462, 563  
 Nipoti, C., Treu, T., & Bolton, A. S. 2009, ApJ, 703, 1531  
 Palacios, A., Gebran, M., Josselin, E., Martins, F., Plez, B., Belmas, M., & Lèbre, A. 2010, A&A, 516, A13  
 Percival, W. J., Cole, S., Eisenstein, D. J., Nichol, R. C., Peacock, J. A., Pope, A. C., & Szalay, A. S. 2007, MNRAS, 381, 1053  
 Ruff, A. J., Gavazzi, R., Marshall, P. J., Treu, T., Auger, M. W., & Brault, F. 2011, ApJ, 727, 96  
 Rusin, D., Kochanek, C. S., & Keeton, C. R. 2003, ApJ, 595, 29  
 Schweizer, F. 1982, ApJ, 252, 455  
 Sérsic, J. L. 1968, Atlas de galaxias australes (Cordoba, Argentina: Observatorio Astronomico)  
 Shu, Y., et al. 2012, AJ, 143, 90  
 Thomas, D., Maraston, C., Bender, R., & Mendes de Oliveira, C. 2005, ApJ, 621, 673  
 Toomre, A., & Toomre, J. 1972, ApJ, 178, 623  
 Treu, T., & Koopmans, L. V. E. 2002, ApJ, 575, 87  
 —. 2004, ApJ, 611, 739  
 Valdes, F., Gupta, R., Rose, J. A., Singh, H. P., & Bell, D. J. 2004, ApJS, 152, 251  
 van der Wel, A., Holden, B. P., Zirm, A. W., Franx, M., Rettura, A., Illingworth, G. D., & Ford, H. C. 2008, ApJ, 688, 48  
 van Dokkum, P. G., Franx, M., Fabricant, D., Kelson, D. D., & Illingworth, G. D. 1999, ApJ, 520, L95  
 van Dokkum, P. G., et al. 2008, ApJ, 677, L5  
 —. 2010, ApJ, 709, 1018  
 Wake, D. A., et al. 2006, MNRAS, 372, 537  
 —. 2008, MNRAS, 387, 1045  
 Warren, S. J., & Dye, S. 2003, ApJ, 590, 673  
 Wayth, R. B., Warren, S. J., Lewis, G. F., & Hewett, P. C. 2005, MNRAS, 360, 1333  
 Wetzell, A. R., & White, M. 2010, MNRAS, 403, 1072  
 White, S. D. M., & Frenk, C. S. 1991, ApJ, 379, 52  
 York, D. G., et al. 2000, AJ, 120, 1579  
 Zirm, A. W., et al. 2007, ApJ, 656, 66